Magnetic shielding of the channel walls in a Hall plasma accelerator

Ioannis G. Mikellides,[*] Ira Katz, Richard R. Hofer, Dan M. Goebel,

Jet Propulsion Laboratory, California Institute of Technology, Pasadena, CA, 91109

and

Kristi de Grys, Alex Mathers

Aerojet, Redmond, WA 98052

Abstract

In a Qualification Life Test (QLT) of a Hall thruster it was found that the erosion of the acceleration channel practically stopped after ~5,600 h. Numerical simulations using a two-dimensional axisymmetric plasma solver with a magnetic field-aligned-mesh reveal that when the channel receded from its early-in-life to its steady-state configuration the following changes occurred near the wall: (1) reduction of the electric field parallel to the wall that prohibited ions from acquiring significant impact kinetic energy before entering the sheath, (2) reduction of the potential fall in the sheath that further diminished the total energy ions gained before striking the material and, (3) reduction of the ion number density that decreased the flux of ions to the wall. All these changes, found to have been induced by the magnetic field, constituted collectively an effective shielding of the walls from any significant ion bombardment. Thus, we term this process "magnetic shielding."

[*]Electronic mail: Ioannis.G.Mikellides@jpl.nasa.gov

I. Introduction

Hall accelerators generate thrust through the formation of an azimuthal electron current that interacts with an applied, quasi-radial magnetic field to produce an electromagnetic force on the plasma. These accelerators provide an attractive combination of thrust and specific impulse for a variety of near-earth missions and, in many cases, they allow for significant reductions in propellant mass and overall system cost compared to conventional chemical propulsion. The range of thrust and specific impulse attainable by Hall thrusters makes them applicable also to a variety of NASA science missions. Many such missions however require wider throttling and longer propellant throughput than near-earth applications.[1,2] A critical risk associated with the application of Hall thrusters to science missions is their throughput capability. There are two major wear processes known to exist in Hall thrusters that can limit their applicability to such missions: erosion of the acceleration channel and erosion of the hollow cathode.

Multiple approaches are being pursued to retire this risk. For example, the high voltage, Hall accelerator (HiVHAc) incorporates an innovative discharge channel replacement technology as a means of extending its life.[3] In 2008 the NASA-103M.XL[4] version of HiVHAc accumulated >4,700 h at 700 V upon the completion of a wear test.[5] More recently, a QLT of a different Hall plasma accelerator, the BPT-4000, was extended beyond 10,400 h.[6] The BPT-4000 is nominally a 4.5-kW class thruster, and has fixed insulators and a magnetic design for high efficiency and long life. Post-test assessment of the wear data showed no measurable erosion of the acceleration channel walls from 5,600 h to 10,400 h indicating that the thruster reached a (near) "steady state" erosion configuration. The QLT results have, potentially, breakthrough implications. They imply that, if properly designed, the life of Hall thrusters can be extended to (or exceed) that of ion thrusters thereby retiring the risk associated with their throughput capability.

The detailed physics that led to this significant reduction of the erosion in the BPT-4000 was not identified upon the conclusion of the QLT. As part of their development of Hall thrusters, the manufacturer of the thruster created a semi-empirical two-dimensional (2-D) erosion model, and has reported excellent agreement with measured erosion profiles.[6] While this erosion model does not capture the detailed physics, the QLT showed that the manufacturer's design[7] provided the basis for efficient operation and very low erosion rates.

The QLT has exceeded significantly the requirements for most commercial or military missions.[8] However, because many NASA science missions require longer operational times, higher throughput, and a wider range of operating conditions, a rigorous understanding of the erosion physics must be attained. Such understanding is important because it must be demonstrated unambiguously that ground test observations of low erosion rates are/were not "anomalous" and that thruster life projections using empirical scalings and/or semi-empirical models alone will be valid (or not) for the more demanding requirements of NASA science missions.

Regarding the aforementioned erosion trends in the BPT-4000, it was recognized early by the authors of this paper that to fully understand such physics one must account, at minimum, for the 2-D distribution of the electric field near the eroding surfaces, the sheath physics, and the local topology of the magnetic field. To account for all these physics, it is required usually that the solution to an extensive system of governing laws for the Hall thruster plasma is obtained, in two or three dimensions. For this reason, we employed initially a 2-D Hybrid-Particle-in-Cell Hall ("HPHall") plasma solver that was developed by Fife and Martínez-Sánchez.[9] The code was upgraded later to HPHall-2 by Parra and Ahedo.[10] Additional algorithm advancements including a new erosion sub-model were also made by several other authors.[11,12,13] Due to its numerical

discretization approach, the HPHall-2 simulations exposed a limitation of the code that prohibited its application to explain the erosion physics in the specific magnetic field topology exposed by the erosion of the BPT-4000 channel in its steady-state configuration. The importance of understanding the erosion physics in such topologies motivated the development of a new Hall thruster plasma solver by the authors of this paper named "Hall2De."[14]

Hall2De is a 2-D computational solver of the laws that govern the evolution of the partially-ionized gas in Hall thrusters. The code is a descendant of OrCa2D, a 2-D computational model of electric propulsion hollow cathodes that employs a mix of implicit and explicit algorithms to solve numerically the plasma conservation laws in these devices.[15,16] In Hall2De, excessive numerical diffusion due to the large disparity of the transport coefficients parallel and perpendicular to the magnetic field is evaded by discretizing the equations on a computational mesh that is aligned with the applied magnetic field. This magnetic field-aligned-mesh (MFAM) capability was largely motivated by the need to assess the life of Hall thrusters in complicated magnetic field topologies.

In this paper we present our findings from Hall2De numerical simulations of the BPT-4000 plasma, which aimed at identifying the physics that led to the erosion trends observed in the QLT. The paper is organized as follows. Section II provides an overview of Hall2De and describes recent physics upgrades that have been implemented in the code. A more detailed description of the code has been provided by Mikellides, et al.[14] Section III discusses comparisons between numerical simulation results and a variety of plasma and performance measurements,[17] in two different geometrical configurations of the acceleration channel. We shall be referring to these configurations hereinafter as the "1200-h" and "steady-state" channel geometries. The two geometries emulate closely the eroded channel walls after ~1200 h of

operation and the "steady-state" erosion configuration, respectively. We shall be referring also to the beginning-of-life (BOL) configuration, which for the purposes of this paper shall represent the nominal geometrical design of this thruster at zero hours of operation. In Section IV we compare computed erosion rates between the 1200-h and steady-state geometries, explain the physics that led to them, and conclude with an assessment of our plasma model uncertainties on our erosion results.

The Hall2De numerical simulations reveal that several changes were induced in the plasma as portions of the magnetic field, buried into the dielectric material in the BOL design of this thruster, became exposed to the plasma. This exposure was caused by the recession of the acceleration channel from its original geometry to its steady-state configuration. Collectively, the induced changes of the plasma properties constituted an effective shielding of the channel walls from ion bombardment. Because all such changes in the behavior of the plasma near the eroding surfaces have been found to be driven by the magnitude and topology of the magnetic field there, we call this wear-reducing mechanism "magnetic shielding."

II.   The 2-D Axisymmetric MFAM Code "Hall2De"

A. General description of the code and motivation behind its development

Because the fundamental principle behind the acceleration of ions in Hall thrusters is based on operating them at high electron Hall parameter ($\Omega_e > 100$), the diffusion of mass and heat for the electron flow in the direction parallel to the magnetic field is much greater (by $\sim \Omega_e^2$) than that in the perpendicular direction for most of the channel region. This leads to the "equipotentialization" and "isothermalization" of the lines of force[18]: streamlines of the magnetic vector field are, approximately, also lines of constant "thermalized" potential $\phi_T \equiv \phi - T_e \ln(n_e)$ and constant electron temperature. This may allow for a computational simplification in

configurations where the magnetic field lines begin at one side of the thruster annulus and end at the opposite side. Specifically, it may be possible to solve for the plasma potential and electron temperature in a (quadrilateral) computational cell that is bounded by two adjacent lines of force rather than one with arbitrary dimensions, and then interpolate the solution onto a an arbitrary structured mesh. This simplification formed the basis for the development of a number of 2-D computational models of Hall thrusters in existence today such as HPHall. HPHall uses a set of quasi-one-dimensional fluid equations for the electrons and a particle-tracking Boltzmann solver for the heavy species in 2-D axisymmetric geometry. The code was developed by Fife and Martínez-Sánchez in the late 90s[9] and since then it has provided invaluable insight into Hall thruster physics at various institutions of academia, industry and government.

When Hall thrusters are operated for thousands of hours excessive erosion may expose magnetic field topologies in which a line of force begins and ends at the same surface rather than traversing the channel annulus. In such regions the discretization approach followed in HPHall cannot be used to simplify the numerical approach for the solution of the electron equations. In such cases, a more generalized discretization approach is necessary or a multiblock approach combining different computational domains where the quasi-one-dimensional fluid equations are solved. Hall2De follows the first. A main challenge with this approach however is excessive numerical diffusion, caused by the large disparity of the transport coefficients in the parallel and perpendicular directions of the magnetic field. This may be avoided by discretizing the equations on a computational mesh that is aligned with the magnetic field. Solution on a MFAM is a long-standing computational approach for simulating highly-anisotropic plasmas (e.g. see Refs. 19, 20, 21, 22, 23).

The MFAM Hall2De has been under development since 2009.[14] The conservation equations, numerical methodology and preliminary simulation results have been presented in detail by Mikellides, et al.[14] Here we provide a brief overview of the code and describe recent physics and numerical upgrades.

---FIGURE---

Fig. 1. Schematic of the computational region and naming conventions for the boundary conditions (BC) in the MFAM code Hall2De.

Although there are many similarities between Hall2De and other hybrid-based codes, there are also several distinctive features in both the physics and the numerical approach. Such features have been incorporated in the code after many lessons learned from Hall thruster simulations over the last decade or so. Due to the long history and wide use of HPHall it may be most instructive to outline the major distinctions between Hall2De and HPHall; there are three:

1) discretization of all conservation laws on a MFAM,

2) numerical solution of the heavy-species conservation equations without invoking discrete-particle methods

    (a)   ions are treated as an isothermal, cold (relative to the electrons) fluid accounting for the drag force and ion-pressure gradient,

    (b)   atomic species (neutrals) are treated as part of a collisionless gas and their evolution in the computational domain is computed using line-of-sight formulations that accounts for ionization,

3) large computational domain that extends several times the thruster channel length in the axial direction, and encompasses the cathode boundary and the axis of symmetry.

The first allows for the assessment of erosion in regions with complex magnetic field topologies. In regions of the thruster where the lines of force retain their isothermal and equipotential properties the main distinction between Hall2De and HPHall regarding computational approach is that in HPHall a computational cell is defined by two lines of force and the solution is then interpolated onto an arbitrary structured mesh, whereas in Hall2De such computational cell would be further divided into additional cells using an orthogonal set of lines. The equations are then solved on each one of these additional cells at the expense of additional computational time but without the need for interpolation onto another mesh. The main advantage here is the ability to simulate regions of the thruster where surfaces have disrupted the lines of force. In a previous series of numerical simulations using the BOL geometry of the BPT-4000, the Hall2De and HPHall solutions were found to be in close agreement within the extent of the HPHall computational domain. The MFAM also allows for the self-consistent simulation of the plasma in the near-anode region; unlike HPHall, there is no magnetic field streamline in this region of Hall2De upstream of which the conservation laws for the plasma are not solved self-consistently. The second eliminates the inherent statistical fluctuations associated with particle-based methods and the third will give us an opportunity in the future to study, among others, purely axisymmetric thrusters where the cathode is positioned at the thruster centerline. A schematic of the Hall2De physical domain with naming conventions for the various boundaries are provided in Fig. 1.

B. Physics, numerical approach and recent augmentations in Hall2De

1) Ions

The evolution of ions in Hall2De is computed using a hydrodynamic approach. It is based on the assumption that the ion gas constitutes an isothermal, cold (relative to the electrons) fluid. The justification and empirical support[24] for the ion-fluid approximation has been discussed by Mikellides, et al.[14] The momentum and continuity equations for the ions account for multiple ionization collisions that include triply-charged ions (Xe^{3+}). A reaction that yields Xe^{3+} from an electron collision with a Xe^+ was recently included in the code. The cross-sectional data for this reaction are provided in Ref. 25. The momentum equation includes the ion pressure-gradient force and the drag force on ions due to their elastic and inelastic collisions with other heavy species in the simulation domain. The code has been updated recently to include contributions from coulomb collisions of ions of different charge states. The ion conservation laws are closed with conditions specified at all boundaries in Fig. 1. At the anode and dielectric-wall boundaries the Bohm condition is prescribed for the speed with which the ions exit the physical domain (i.e. at entry to the sheath).

Specifically, the marginal condition for the hydrodynamic Bohm criterion is imposed at the boundary $u=(k_B T_e/m_i)^{1/2}$ for ions, which assumes cold mono-energetic ions and Bolzmann-distributed electrons in the sheath, with fully absorbing walls. This is a limiting condition when the ion flow velocity is less than the ion acoustic speed, and does not take into account contributions of low-energy ions in the ion velocity distribution function (e.g. see Ref. 26). However, as it will be shown by the erosion rate comparisons between the two channel geometries, the conclusions of this article regarding the fundamental principle behind magnetic shielding are expected to remain unchanged with a more rigorous implementation of the Bohm criterion (e.g. see Refs. 27 and 28); the shielding effect is a large-scale effect (by comparison to the sheath physics) that alters the bulk plasma conditions in the vicinity of the channel walls. At

the plume boundaries the ions are allowed to flow out of the system freely (gradients of the two velocity components are set to zero). Reflection boundary conditions are set at the axis of symmetry.

Hall2De solves numerically the non-conservative form of the ion momentum equation using a first-order upwind scheme. The equation is marched forward in time explicitly. The velocities are defined at the vertices of each quadrilateral computational cell. Bilinear interpolation is used to define forces at vertices from their primitive values at the cell edges and to define scalar quantities at vertices from their primitive values at the cell centers.

2) Electrons

The electron population in Hall2De is treated as an inviscid fluid. The electron momentum equation in is given by

$$n_e m_e \frac{D\mathbf{u}_e}{Dt} = -en_e \left(\mathbf{E} + \mathbf{u}_e \times \mathbf{B} \right) - \nabla p_e + \mathbf{R}_e \tag{1}$$

where the friction force $\mathbf{R}_e/n_e$ is related to the integral of the collision term in the electron distribution function and the electron momentum. In Eq. (1) the electron number density and mass are n_e and m_e, respectively, $\mathbf{u}_e$ is the electron drift velocity, e is the electron charge, $\mathbf{E}$ is the electric field, $\mathbf{B}$ is the magnetic induction field, and p_e is the electron pressure. In the absence of high-frequency electron dynamics the electron inertia may be neglected. Then one obtains the vector form of Ohm's law as follows:

$$E_{\|} = \eta j_{e\|} - \frac{\nabla_{\|} p_e}{en_e} + \eta_{ei} j_{i\|} \qquad\qquad E_{\perp} = \eta \left(1 + \Omega_e^{\,2} \right) j_{e\perp} - \frac{\nabla_{\perp} p_e}{en_e} + \eta_{ei} j_{i\perp}, \tag{2}$$

expressed here in the frame of reference of the magnetic field (with "$\|$" and "$\perp$" denoting parallel and perpendicular components, respectively). The electron (ion) current density is denoted by $j_{e(i)}$ and the total resistivity of the plasma is η; η_{ei} includes only the electron-ion contribution to the

resistivity. The electron Hall parameter is $\mathbf{\Omega}_e$. Equations (2) imply the approximation $\mathbf{u}_e \gg \mathbf{u}_n$. The resitivity includes the contributions from collisions of electrons with all other species. Equations (2) imply also that there are sufficient collisions to sustain the equilibrium distribution function for the electrons in each direction relative to the magnetic field. Estimates of the minimum collision mean free path for electrons inside the acceleration channel suggest that the collisionality of the species parallel to the magnetic field may be insufficient to warrant the continuum form of Ohm's law as expressed by the left of Eqs. (2). Our simulations confirm however that the resistive terms in the parallel direction are negligible compared to the remaining terms. Then effectively, we have $E_\parallel \approx \nabla_\parallel p_e / e n_e$, which yields the expected dependence of the plasma potential (ϕ) on the electron temperature (T_e) and n_e in the parallel direction. The same arguments apply to the electron energy equation (to be presented later) yielding the expected (near) "isothermalization" of the lines of force, i.e. $\nabla_\parallel T_e \approx 0$. Thus, although parallel to the magnetic field we use classical thermal conductivity for the electrons, $\kappa_{e\parallel} \propto n_e T_e / \nu_{e\parallel}$, where $\nu_{e\parallel}$ denotes total classical collision frequency with contributions from electron-ion, electron-neutral and electron-wall collisions, the precise model is of little significance inside the acceleration channel. From this viewpoint, each computational cell in Hall2De then is analogous to one computational "zone" in HPHall. In HPHall, such "zones" are defined by four edges; these edges are the two adjacent lines of force and the two boundary edges each located at opposite wall boundaries.

It has also been suggested that the diffusion of electrons in Hall thrusters is enhanced in a non-classical manner by plasma turbulence (e.g. see Refs. 9, 29, 30, 31). Many attempts to capture this enhancement in numerical simulations with HPHall and similar codes have been made through the use of an effective collision frequency, which we term here "ν_α". Fife and

Martínez-Sánchez proposed originally[9] that ν_α in Hall thrusters may be based on Bohm's 1/B scaling for the cross-field mobility,[32] and used a coefficient α to enhance the total collision frequency for the electrons while retaining the proportionality of ν_α with ω_{ce}. A similar approach has been followed by others (e.g. see Ref. 31). In this paper we have imposed the generalized function

$$\nu_\alpha = \alpha(r,z)\omega_{ce}, \tag{3}$$

allowing α to vary spatially in the simulation region. As we shall show later in the paper numerical simulations with Hall2De that were guided largely by plasma data suggest large deviations of α from a constant value and therefore little to no correlation of ν_α with ω_{ce}.

During their azimuthal drift electrons collide with walls also. This was proposed (originally by Morozov[18]) to be one more process that affects the transport of electrons in the acceleration channel. In numerical simulations of Hall thrusters this additional transport mechanism has been accounted for through the addition of another effective collision frequency, ν_{ew}, that is dependent upon the electron secondary yield. In Hall2De the collision of the electrons with the walls is similar to that used in HPHall but is accounted for at the collision site only. Previous simulations with Hall2De that incorporated ν_{ew} precisely as it is implemented in HPHall did not show significant impact on BPT-4000 simulation results.[14] In Section III-A we provide comparisons of the collision frequencies at the channel centerline and along the wall boundaries. Accounting then for all transport mechanisms the electrical resistivity and the Hall parameter are determined as follows:

$$\eta = \frac{m_e \nu_e}{e^2 n_e} \qquad \Omega_e = \frac{|B|}{e n_e \eta} \tag{4}$$

where ν_e is defined as

$$\nu_e \equiv \nu_{ei} + \nu_{en} + \nu_{ew} + \nu_\alpha. \tag{5}$$

The first two terms on the right of Eq. (5) are the classical (total) electron-ion and electron-neutral collision frequencies.

The electron energy conservation law is solved for the electron temperature (expressed in eV) and is given by

$$\frac{3}{2}en_e\frac{\partial T_e}{\partial t} = \mathbf{E}\cdot\mathbf{j}_e + \nabla\cdot\left(\frac{5}{2}T_e\mathbf{j}_e + \boldsymbol{\kappa}_e\cdot\nabla T_e\right) - \frac{3}{2}T_e\nabla\cdot\mathbf{j}_e - \sum_s \Phi_s + Q_e^T \tag{6}$$

where κe is the electron thermal conductivity and includes components parallel and perpendicular to B. The last term on the right represents the energy exchange per unit time between electrons and the heavy species[33] due to deviations from thermal equilibrium, and usually in Hall thrusters, they constitute a small contribution to the total electron energy. Inelastic energy losses are accounted for by the terms in the sum, $\Sigma\Phi_s$, and include ionization as well electron excitation losses.[34] Presently, excitation losses account only for ground-state transitions.

The equations for the electrons are closed with boundary conditions (BC) at all surfaces in Fig. 1. At the anode, a Dirichlet condition specifies directly the voltage at its discharge value and imposes that the normal component of the electric field vanishes inside the conductor. For the simulation cases that are presented in this paper this value is 300 V. More recently we updated Hall2De with sheath BCs for the electron current density normal to the anode: $j_e = -j_{Te}\exp[-e(\phi-V_A)/k_BT_e]$ for $\phi > V_A$ (electron repelling sheath) where $j_{Te} = en_e(8k_BT_e/\pi m_e)^{1/2}/4$ is the electron thermal current density and k_B is Boltzmann's constant. The new formulation is employed in an implicit fashion in the potential solver. We have found that the major distinction between the two BCs (Dirichlet versus sheath) is the production of a higher plasma potential near the anode when

sheath BCs are employed, which is to be expected since the electron thermal current density integrated over the anode area is much higher than the discharge current in these devices. We found no major differences downstream of the anode that would alter our conclusions on erosion. At the cathode boundary we specify directly the plasma conditions there for the neutral particle flux, ion flux, plasma potential and electron temperature. All such conditions are guided by independent numerical simulations of the actual cathode flow from the orifice (e.g. see Ref. 35). For the convective heat flux (j_eT_e) normal to the anode Hall2De employs sheath BCs assuming an electron-repelling sheath. Such BCs have been described numerous times elsewhere (e.g. see Ref. 36). For all dielectric-wall boundaries a zero-current condition is imposed. For the electron energy BCs at these boundaries the convective heat loss follows the formulations of Hobbs and Wesson[37] regarding the potential drop in the sheath with secondary electron emission. The energy equation is solved in a semi-implicit fashion; the thermal conduction term is implicit whereas all other terms are evaluated at the previous time-step.

The numerical approach followed in Hall2De for the electrons is to solve the electron equations in the frame of reference of the magnetic field, in two dimensions. Specifically, the plasma potential is solved by combining the equation for current conservation and Ohm's law into one equation and discretizing on a computational mesh that is aligned with the magnetic field lines.[14] The equation is solved implicitly. Numerical diffusion is reduced by assuming that cell edges are exactly either parallel or perpendicular to the magnetic field lines (Fig. 2 middle). The accuracy of the solution is then dependent upon the extent of the spatial deviations of the mesh from the true lines of constant potential and stream functions χ and ψ. Here, χ and ψ are the commonly-used set of conjugate harmonic functions satisfying the Cauchy-Riemann conditions for the radial and axial components of the magnetic field. A set of such lines in the

vicinity of the acceleration channel of a 6-kW laboratory Hall thruster[38,39,40] are shown in Fig. 2 left. The corresponding MFAM for this thruster is shown in Fig. 2 right. In Fig. 3 we show computed electron temperature contours in the vicinity of the acceleration channel in the 6-kW thruster. The contours are overlaid by streamlines of the magnetic field to demonstrate that Hall2De preserves the isothermalization of the lines of force, a well-known feature of conventional Hall thrusters (like the 6-kW Hall thruster and the BPT-4000). We emphasize that the 6-kW thruster and the BPT-4000 are different Hall thrusters, employing, among others, different magnetic field topologies.

---FIGURE---

Fig. 2. Left: A set of lines of constant stream function (ψ) in blue (streamlines of the magnetic field) overlaid by lines of constant potential function (χ) in red, in the vicinity of the acceleration channel in a 6-kW laboratory Hall thruster. We note that the magnetic field topology and geometry of this thruster are different than those of the BPT-4000. Middle: Each edge of a computational cell in Hall2De is closely aligned with either a χ-line or a ψ-line. Right: corresponding finite-element computational mesh.

---FIGURE---

Fig. 3. Hall2De preserves the isotheral properties of the lines of force, a well-known feature in conventional Hall thrusters like the 6-kW Laboratory Hall thruster and the BPT-4000. The plot shows computed electron temperature contours overlaid by selected lines of constant stream function ψ (i.e. streamlines of the magnetic field) in a 6-kW laboratory Hall thruster.

3) Neutrals

The neutral gas in most Hall thrusters is in the free-molecule regime. An algorithm that is not based on discrete-particle statistics was developed for Hall2De to determine the density of neutrals.[41] The algorithm takes advantage of the fact that almost all neutral particles in this rarefied medium proceed along straight-line, constant-velocity trajectories until they are either ionized, strike a wall, or leave the physical domain. The algorithm assumes that the particle velocity distribution function for neutrals emitted from a given surface remains unchanged except for a scale factor that reflects the loss of neutrals to ionization. Then the algorithm solves for the neutral gas density by integrating forward in time the linear Boltzmann equation in the absence of any forces on the particles. The sources of neutrals are gas inlets and isotropic, thermally-accommodated gas molecules emanating from chamber surfaces including recombined ions. Compared with the particle methods, commonly used in many plasma simulation codes like HPHall, this algorithm achieves "quiet" and smooth solutions.[41]

III.   Comparisons of Numerical Simulation Results and Measurements

In this section we present comparisons between simulation results and plasma measurements at various locations in the plume of the thruster. The plasma diagnostics and a more detailed description of the measurements are provided by Hofer, et al.[17] In Section III-A we describe the channel geometries simulated, and present our comparisons for the electron temperature and plasma potential along various axial and radial slices in the thruster plume. We also present in this section comparisons with the measured performance. Section III-A concludes with a presentation of selected 2-D results and explanations of the significance of the computed trends near the walls. In Section III-B we discuss the comparisons between theory and experiment in greater detail and identify areas in our theoretical efforts that will be the focus of future investigations.

A. Comparisons in the 1200-h and steady-state channel geometries of the BPT-4000

We have employed Hall2De to simulate the plasma and erosion in the BPT-4000 with the goal of understanding the mechanism(s) that led to the reduced erosion rates in the QLT. Our approach has been to simulate two different channel geometries, one emulating the thruster configuration early in the QLT and one late in the QLT, and then compare the erosion rates. In reference to the numerical simulation results, throughout this and subsequent sections we shall be alluding to three different configurations of the BPT-4000 acceleration channel: (1) beginning-of-life (BOL) geometry, (2) 1200-h geometry and (3) steady-state geometry. In the simulations the 1200-h geometry resembles closely the shape of the channel walls after 1200 h of operation of the thruster in the QLT.[6] The steady-state geometry emulates closely the shape of the channel after 5,600 h; beyond this time recession of the walls by erosion had practically ceased. The three different channel geometries and reference scale lengths are depicted in Fig. 4.

---FIGURE---

Fig. 4. Schematic of the BPT-4000 acceleration channel showing the 1200-h and steady-state geometries as used in the Hall2De numerical simulations. Also shown for reference is the BOL geometry. The simulations used a mesh that was aligned with the magnetic field in BPT-4000.

Despite more than two decades and numerous investigations in the United States and other western countries, the true physics of the diffusion of electron heat and particle flux across magnetic field lines in conventional Hall thrusters remain elusive. Because the solution to this long-standing problem is beyond the scope of this effort our approach here has been to seek spatial variations of the non-classical collision frequency $\nu_\alpha(r,z)$ that are guided by the plasma measurements. Our approach is similar to that followed by Hagelaar, et al.[42,43]

We present below four simulation cases: three for the 1200-h geometry and one for the steady-state geometry. Each case is associated with different functions $\nu_\alpha(r,z)$. To sustain a stable solution, Ω_e in regions of the plume was also modified and this is discussed in greater detail in Refs 14 and 34. Functions $\nu_\alpha(r,z)$ for the three cases in the 1200-h geometry are plotted in Fig. 5 along the channel centerline. Also plotted in Fig. 5 left and in Fig. 6 are the remaining collision frequencies comprising ν_e (see Eq. REF). We note in Fig. 6 that near the dielectric, electron collisions with walls can dominate the total collision frequency for a large extent of the channel. The large drop of ν_{ew} beyond z/L for the inner channel wall compared to the outer wall seen in Fig. 6 is associated with the larger values of the magnetic field near the inner surface, which in turn yield larger ν_α. These larger values are more clearly depicted in the 2-D contour plots of Fig. 7 comparing ν_α (left) and ν_e (right) for case 1.

---FIGURE--

Fig. 5. Numerical simulation results of the relevant frequencies along the channel centerline of the 1200-h geometry (cases 1-3 of the simulations). Each case corresponds to different profiles of ν_α as imposed in the simulations.

---FIGURE--

Fig. 6. Contributions of electron collisions with the channel walls to the total collision frequency ν_e. The collision frequency ν_{ew} is implemented in Hall2De at the computational cells adjacent to the dielectric wall boundaries, as indicated in the schematic to the left. This allows us to account for the "near-wall" conductivity in this thruster. The right plot shows the ratio of ν_{ew} over the

total collision frequency ν_e, which includes ν_α, along the outer and inner boundaries inside the acceleration channel.

---FIGURE---

Fig. 7. Contours of the non-classical collision frequency ν_α (left), implemented in the numerical simulations of the BPT-4000 for case 1, compared to the total collision frequency ν_e (right). ν_e accounts for classical coulomb collisions between electrons and ions, electron-neutral collisions and near-wall collisions.

The simulation solutions of the electron temperature and plasma potential for all three cases along the channel centerline in the 1200-h geometry are compared with the plasma measurements in Fig. 8. Despite the differences between the imposed frequency ν_α, all three cases are found to yield results that are within or close to the experimental uncertainty of the plasma measurements. Regarding thruster performance and related integrated parameters, the 1200-h simulation results are within 3% of the measured thrust (see Table 1). The most noticeable discrepancies are associated with the thruster currents. Specifically, we found a consistent over prediction of the Xe^{2+} ion current fraction and an under prediction of the Xe^+ fraction. These and other discrepancies between theory and experiment are discussed in Section III-B.

---FIGURE---

Fig. 8. Comparisons between numerical simulation results and axial plasma measurements obtained along the channel centerline (r/R=1) in the 1200-h geometry of the BPT-4000. Left: electron temperature. Right: plasma potential.

---TABLE---

Table 1. Performance comparisons between numerical simulation results and measurements in the 1200-h and steady-state channel geometries of the BPT-4000.

Radial comparisons between the computed results and plasma measurements have also been performed. These comparisons are shown in Fig. 9 for three axial locations in the 1200-h geometry. The top-left figure shows contour plots of the plasma potential for case 1. The three radial slices along which the comparisons are made are also plotted as dashed lines. The top-right plot is the comparison closest to the acceleration channel, at z/L=1.113, followed by z/L=2.088 (bottom-left) and z/L=4.715 (bottom-right). The simulation predicts well the plasma potential within approximately a channel height in front of the acceleration channel but the agreement diminishes at greater angles relative to the thrust vector. This discrepancy is discussed in Section III-B.

---FIGURE---

Fig. 9. Comparisons between numerical simulation results and radial measurements of the plasma potential in the 1200-h channel geometry of the BPT-4000. Top-left: computed contours of the plasma potential for case 1 showing radial slices along which the comparisons between theory and experiment have been performed. Top-right, bottom-left and bottom-right: comparisons at z/L=1.113, 2.088 and 4.715, respectively.

Similar comparisons between theory and experiment are presented below for the steady-state channel geometry. Fig. 10 left plots the relevant collision frequencies along the channel centerline including the imposed profile for ν_α; we shall refer to this simulation as "case 4." The axial comparisons between theory and experiment for this case are depicted in Fig. 11.

---FIGURE---

Fig. 10. Numerical simulation results along the channel centerline in the steady-state geometry (case 4 of the simulations). Left: relevant frequencies.

---FIGURE---

Fig. 11. Comparisons between numerical simulation results and axial plasma measurements obtained along the channel centerline (r/R=1) in the steady-state geometry of the BPT-4000. Left: electron temperature. Right: plasma potential. Method 1: directly from Langmuir probe traces. Method 2: derived from emissive probe measurements.

The radial comparisons at two different axial locations downstream of the channel exit, z/L=1.188 and 1.525, are plotted in Fig. 12. The comparison in Fig. 12 left is of particular interest since both theory and experiment display a non-monotonic profile of the electron temperature with radius. In light of the isothermalization of the field lines, the significance of this trend is that such non-monotonicity is expected at this proximity to the channel exit due to the magnetic field topology there. It is also observed that the numerical simulation predicts a profile that is very similar, both qualitatively and quantitatively, to the measurement but at a different location relative to the channel. The spatial discrepancy is of the order of a few millimeters and may have been caused by differences between the magnetic field model used in the simulations and the real field applied in the thruster. Also, cumulatively, probe-thruster misalignments are estimated to be of the order of 1-2 mm.

---FIGURE---

Fig. 12. Comparisons between numerical simulation results and radial measurements of the electron temperature obtained at two different locations, z/L=1.188 (left) and z/L=1.525 (right), downstream of the acceleration channel in the steady-state geometry of the BPT-4000. The left

and right vertical lines on each plot indicate the radial locations of the inner and outer walls of the channel's cylindrical section, respectively.

Contour plots are compared for the 1200-h and steady-state geometries in Fig. 13. The effect of the equipotentialization of the lines of force[18] is shown clearly in Fig. 13 top. For example, we found only a 30-V reduction (275 to 245 V) along the outer diverging wall of the steady-state configuration compared to a significant drop of 286 V in the 1200-h geometry. Thus, acceleration of ions along the diverging wall in the 1200-h is considerably higher compared to the steady-state geometry. This higher acceleration, in turn, increases the kinetic energy with which ions enter the sheath.

The same principle that leads to the equipotentialization of the lines of force is responsible also for their isothermalization. Thus, since lines of force are nearly isothermal in the acceleration channel, the lines that graze the corner formed by the cylindrical and diverging sections of the channel wall in the steady-state geometry are associated also with low values of the electron temperature since these lines extend deep into the acceleration channel. There, the electrons are considerably cooler (see also Fig. 11 left). For the BPT-4000 channel this is shown in Fig. 13 middle comparing contours of the electron temperature in the 1200-h and steady-state geometries. The comparison shows a reduction in the maximum temperature, as much as seven times along the diverging walls. Because the electron temperature was reduced significantly along the diverging walls in the steady-state geometry, a reduction in the sheath drop across these surfaces was also induced. Thus, ions acquire less kinetic energy inside the sheath before striking the wall.

A third effect seen in the steady-state geometry is largely related to the plasma potential profile. Specifically, because the component of the electric field parallel to the diverging section

of the dielectric is marginalized in the steady-state geometry, the acceleration of ions is mostly axial and away from the wall. This is shown by the representative velocity streamlines of Xe^+ overlaid on the electron number density contours in Fig. 13 bottom. Thus, the radial expansion of the plasma beyond the cylindrical section of the accelerator is reduced compared to that in the 1200-h geometry, and the region near the diverging wall of the steady-state geometry is populated by a much lower number of charged particles. The electron number density is found to be more than one order of magnitude less in the steady-state geometry than in the 1200-h geometry. The significance of this on erosion is that the total flux to the wall is reduced drastically also.

B. Discussion of the comparisons between theory and experiment

The wide range of comparisons between thruster measurements and numerical simulations we performed establish the state of the validation of Hall2De and identify areas in Hall2De's physics models that require further improvement. The most evident need for better understanding is associated with the fact that a different profile of the collision frequency ν_α must be prescribed in different channel geometries and/or operating conditions. This implies that Hall2De is not yet a fully-predictive code for Hall thrusters. This has been a long-standing challenge in the numerical simulation of Hall thrusters that is now more than two decades old.

As a precursor to a more detailed interrogation on this subject we performed a series of sensitivity simulations with different profiles of the collision frequency ν_α to identify region(s) that deviate most significantly from classical transport. The intent was to seek functional dependencies of this "non-classical" frequency (as guided by the measurements) that could lead us to first-principles formulations of the true transport physics. Our sensitivity simulations with different profiles in the 1200-h geometry show that different functional forms of ν_α can produce

similar solutions for the plasma and thruster performance. This presents a challenge in our quest of the true electron transport physics because different spatial variations of ν_α – all yielding results that are either within or close to the experimental uncertainty of plasma measurements, thrust and discharge characteristics of the thruster – make correlations with true frequencies ambiguous. For example, by comparison to the electron cyclotron frequency or the Bohm ($\nu_B=\omega_{ce}/16$) collision frequency (see Fig. 5 and Fig. 10), we found no functional similarities with the imposed ν_α that span both the acceleration channel and the near plume. Noted is the comparison of the frequencies inside the channel: although ν_α for case 3 is directly proportional to ω_{ce} ($\propto B$), cases 1 and 2 fall faster with decreasing magnetic field inside the channel. Outside the channel we found ν_α to differ significantly from ν_B in peak magnitude *and* spatial variation, in both the 1200-h and steady-state channel geometries. Thus, although electron collisions other than those associated with classical particle interactions (such as collisions with the thruster walls) may indeed lead to distinctive transport trends, we found no correlations between ν_α and ν_B, and are unable to identify distinct regions of this problem that can be linked unambiguously with different fractions of ν_B.

The radial comparisons in Fig. 9 identify regions where the behavior of the plasma remains elusive. Specifically, we found that although the imposed profiles lead to good agreement with the plasma potential measurement near the channel centerline, the agreement begins to diminish away from it in the radial direction. In these high-angle regions of the thruster plume the simulation results simply reflect the expected variation of the plasma potential there as the low-density ion beam converges onto the thruster centerline. The computed gradient of the plasma potential in the radial direction as depicted in Fig. 9 is, therefore, not surprising. However, the measurement (also shown in Fig. 9) suggests a different trend with radius. This trend is most

evident in the z/L=1.113 and 2.088 locations and 0<r/R<0.75, i.e. in the inner regions of the

plume closest to the thruster walls. Of particular interest is the negligible radial electric field

measured at the thruster centerline, which implies the presence of low-energy plasma. Using the

measured values of the plasma potential and electron temperature[17] for z/L=1.113, and the

computed values of the plasma density at the channel centerline we estimate that the density one

would expect to have in these regions of discrepancy between theory and experiment is

approximately 3.5×10^{16} m^{-3}.[34] This value is approximately two orders of magnitude higher than

the computed value of $\sim 5.2 \times 10^{14}$ m^{-3} at this location. Low-energy charge-exchange ions are a

possible source for this discrepancy. Presently, such ions are not treated as distinct species in

Hall2De and as a result their concentration may be underestimated significantly in these regions

of the thruster. Enhanced ionization not accounted for by the inelastic models in Hall2De and/or

electrons from regions of the far plume that extend outside of our computational domain are

other candidates for the discrepancy. For example, as discussed in Katz, et al.,[44] most of the

electrons that leave the hollow cathode proceed to neutralize the ion beam and only a small

fraction of them enter the channel. Presently, the Hall2De far-plume BCs impose current

neutrality. This condition requires electrons leave the computational region at the same location

as the ions. Since the ions are not magnetized many electrons are forced across field lines to

neutralize the beam. This current generates a non-negligible electric field because it is multiplied

by Ω_e^2. It is possible that the paths of these electrons extend far outside the Hall2De

computational grid and beam current neutralization occurs meters downstream of the thruster

exit plane. If so, regions in the Hall2De plume that predict presently finite electron current

density could sustain negligible flow of electrons, which would marginalize the contributions of

the resistive electric field in these regions. Current neutralization far down stream of the channel

exit is consistent with published data showing that hollow cathode coupling improved when the cathode was far from the thruster.[45] We plan to investigate this in the future by using a much larger computational region.

Regarding the comparisons related to thruster performance in Table 1, Hall2De appears to yield higher electron temperature than the values expected inside the BPT-4000 channel based, for example, on the ion current fractions. Presently, these fractions are over predicted by the code for Xe^{2+} and under predicted for Xe^{+}. Wall emission/absorption characteristics and related sheath physics have been the subject of investigation for several years [e.g. see Refs. 46, 47, 48, 49 and 50], and is an area we plan to re-visit in the near future since such physics may affect our simulation results in the channel and plume regions.

The one-on-one comparisons with the BPT-4000 measurements have identified areas of improvement in the Hall2De physics, mostly associated with the plume regions of this thruster, but have also allowed us to obtain plasma solutions for the two channel geometries that permit detailed assessments of the erosion rates in this thruster. The impact that our uncertainties in the plasma solution may have on the determination of the erosion rates is discussed in Section IV-B.

---FIGURE---

Fig. 13. Comparison of the numerical simulation results in the 1200-h (left) and steady-state (right) channel geometries. Top: Plasma potential. Middle: Electron temperature. Bottom: Electron number density overlaid by representative trajectories of singly-charged ions.

IV. Erosion of the Acceleration Channel

A. Determination of the erosion rates

The sputtering erosion rate ε due to ion bombardment is given by,

$$\varepsilon = j_{i\perp} Y \tag{1}$$

where the incident ion current density perpendicular to the channel wall $j_{i\perp}$ is dependent on the ion number density n_i and the ion velocity at the wall $u_{i\perp}$. The sputtering yield of the channel material Y is a function of the ion impact energy and incidence angle θ. Because ions must traverse a sheath at the wall before striking it, the total impact energy is the sum of the kinetic energy K_p ions have acquired in the plasma upon entrance to the sheath, and the kinetic energy K_s ions can acquire as they are accelerated further inside the sheath with potential energy $\Delta\phi$. These dependencies may be expressed as

$$j_{i\perp} = j_{i\perp}(n_i, u_{i\perp}) \qquad\qquad Y = Y(K_p + K_s, \theta). \tag{2}$$

$\Delta\phi$ is computed based on the solution to the one-dimensional sheath equations in the presence of secondary electron emission. Hobbs and Wesson[37] showed that a system of three non-linear equations for the electric field $\bar{E}_w$ and sheath potential φ_w at the wall, and the ion Mach number M, may be obtained as written below in dimensionless form:

$$\bar{E}_w{}^2 = \left(-\frac{d\varphi}{d\xi}\bigg|_w\right)^2 = 2M^2\left[\left(1-\frac{2\varphi_w}{M^2}\right)^{\frac{1}{2}}-1\right] - \frac{S}{S-S}\left(-8\mu\varphi_w M^2\right)^{\frac{1}{2}} + 2\left(e^{\varphi_w}-1\right)\left[1-\frac{S}{1-S}\left(-\frac{\mu M^2}{2\varphi_w}\right)^{\frac{1}{2}}\right]$$

$$\varphi_w = -\ln\left[\frac{1-S}{M(2\pi\mu)^{\frac{1}{2}}}-\frac{S}{\left(-4\pi\varphi_w\right)^{\frac{1}{2}}}\right] \tag{3}$$

$$M^2 = 1 + \frac{S}{1-S}\mu^{\frac{1}{2}}\left(-\frac{M^2}{2\varphi_w}\right)^{\frac{3}{2}}(1-2\varphi_w)$$

with normalized variables defined as

$$\xi \equiv x\left(\frac{e^2 n_e}{\varepsilon_0 k_B T_e}\right)^{\frac{1}{2}} \qquad \varphi \equiv \frac{e\Delta\phi}{k_B T_e} \qquad M \equiv \frac{u_0}{\sqrt{k_B T_e / m}} \qquad \mu \equiv \frac{m_e}{m} \tag{4}$$

In Eq. (4) the distance from the wall is x, the ion velocity at the sheath edge is u_0, m is the ion mass, and ε_0 is the permittivity in vacuum. For ease of computation in the numerical simulations we employ a fit[51] of the Hobbs and Wesson solution to Eqs. (3). The secondary electron yield for the BPT-4000 channel material is approximated by,

$$S = S_0 + (1 - S_0) \frac{T_e}{K_{e0}/2} \qquad (5)$$

where $S_0 = 0.54$ and the Maxwellian cross-over is $K_{e0}/2 = 20$ V. In the simulation we use the vertex-centered ion velocities and the cell-centered ion density at each computational cell adjacent to the wall boundary to determine the total impact energy $K = K_p + K_s$ and θ. Then the sputtering yield is determined using the fitting functions f_K[52] for the energy dependence at zero angle of incidence and f_θ[53] for the angle dependence, as follows:

$$Y(K, \theta) = f_\theta f_K$$
$$f_\theta(\theta) = 1 + c_0 [1 - \cos(c_1 \theta)]^{c_2} \qquad f_K(K) = c_3 \sqrt{K} \left(1 - \sqrt{K_T/K}\right)^{5/2} \qquad (6)$$

with the constants given by $c_0 = 0.52663$, $c_1 = 2.60506$, $c_2 = 1.53462$, $c_3 = 0.0023$ and $K_T = 5.1$. The last value denotes the threshold energy for the material and for $K < K_T$ it is assumed that sputtering does not occur. The fitting functions in Eq. (6) have been used in the past in HPHall simulations that produced erosion results early in the life of the BPT-4000 in close agreement with the QLT observations.[12]

The erosion rates have been computed at three different locations along the diverging section in the 1200-h and steady-state geometries of the BPT-4000 channel. The three locations are denoted "U", "M" and "D" for upstream, middle and downstream points, respectively. The relevant schematic is shown in Fig. 14. The erosion rates and all relevant parameters that led to their determination are tabulated in Tables 2 and 3.

---FIGURE---

Fig. 14. Locations along the diverging dielectric walls of the BPT-4000 where erosion rates have been assessed and tabulated by the numerical simulations (see Tables 2 and 3).

B. Discussion of the erosion results

The results of Section IV-A showed that a significant reduction of the erosion in the steady-state geometry occurred by comparison to the 1200-h geometry. In this section we discuss the driving physics the led to this reduction. We found that the process that led to the erosion trends was in fact multifaceted. That is, several changes occurred in the plasma and magnetic field as the channel receded from its BOL geometry to its steady-state configuration that, when acting collectively, led to an effective shielding of the channel walls from energetic-ion bombardment.

It was as early as the 1960s that the equipotentialization of the lines of force in Hall thrusters led to the realization that the geometry of the lines could be shaped convex toward the anode to provide repulsion of ions from the walls by the electric field, thus reducing the channel erosion.[18] Many thruster designs since then have been guided by this principle yet wall erosion has persisted especially near the channel exit. The BOL configuration of the BPT-4000 is one such example. However, we argue here that in the steady-state configuration of this thruster the local topology of the magnetic field led to distinctive features in the plasma near the wall that extend beyond just repulsion of ions away from the surfaces. Also, we identify in this section distinctions between shielding in the Hall thruster against other devices like the Highly Efficient Multistage Plasma Thruster (HEMP-T)[54] and the Diverging Cusped Field Thruster (DCFT),[55] which employ multi-cusped magnetic field configurations to reduce wall erosion.

We refer to the schematics in Figs 15 and 16 to illustrate the first-principles physics of magnetic shielding in conventional Hall thrusters. Magnetic shielding does not require that magnetic lines are parallel to the wall. However, shielding *can* be achieved if the magnetic lines

are parallel to the wall. In Figs 15 and 16 we show schematically several configurations to clarify our point. For example, in Fig. 15 in the middle schematic, the lines are nowhere close to being parallel to any of the surfaces yet this configuration would provide significant shielding of the surfaces from erosion. In the schematic on the right the lines are near parallel to the diverging section of the wall and this configuration too would provide significant shielding of the diverging wall section. By contrast, the field topology relative to the walls at the channel exit in the left and right configurations of Fig. 16 does not provide any significant shielding from erosion even though lines of force are made near-parallel to that section of the wall.

---FIGURE---

Fig. 15. Left: Typical profile of the non-dimensional plasma potential $\varphi \equiv \phi/\phi_{max}$ and electron temperature $\theta \equiv T_e/T_{e,max}$ along the acceleration channel centerline. Middle and right: Configurations with strong magnetic shielding of the (shaded) walls near the channel exit. The three numbered locations at the centerline correspond to $\varphi_1 \approx \varphi_2 \approx 1$, $\theta_1, \theta_2 << 1$ and $\varphi_3 << 1$, $\theta_3 \approx 1$. The magnetic field topologies, shown here for illustration only, are freehand drawings and do not match topologies in any specific thruster discussed herein.

---FIGURE---

Fig. 16. Configurations with weak or no magnetic shielding of the (shaded) walls near the channel exit. Referring to the generic profiles for φ and θ in Fig. 15 (left), the three numbered locations at the centerline correspond to the following. Left and middle: $\varphi_1 \approx 1$, $\theta_1 << 1$, $\varphi_2 << 1$, $\theta_2 \approx 1$, $\varphi_3 << 1$, $\theta_3 \lesssim 1$. Right: $\varphi_1 \approx \varphi_2 \approx 1$, $\theta_1, \theta_2 << 1$ and $\varphi_3 << 1$, $\theta_3 \approx 1$. The magnetic field topologies, shown here for illustration only, are freehand drawings and do not match topologies in any specific thruster discussed herein.

The key aspect to magnetic shielding as described in this article is the following: of utmost importance is *which* lines of force are in the proximity of the wall. This aspect is also what makes this process unique in Hall thrusters versus other devices like HEMP or the DCFT. In the multi-cusped magnetic field configurations of HEMP or the DCFT the reduction of plasma near the walls is driven by the magnetic mirror effect on the electrons at the cusps. The cusped arrangement provides also the magnetic field direction required to induce the azimuthal electron motion and, consequently, the accelerating electric field in the cusped regions. In the Hall thruster configuration with shielded channel walls there is no magnetic-mirror effect because there are no cusps; the effectiveness of the shielding is dependent upon which line(s) graze(s) the wall. By "which" we refer to which thermalized potential and which electron temperature each line is associated with. Those lines associated with higher potential and lower temperature would shield the walls more effectively than those with lower potential and higher temperature. For example, referring to Fig. 16 left, the variation of the plasma potential along the line associated with point #2 on the centerline is much greater than that associated with point #1 due to the constancy of $\phi - T_e \ln(n_e)$ along each line. The consequence is that ions along that surface can strike the wall with greater kinetic energy as they fall through a greater potential drop along that surface. Also, unless the sheath is approaching the space charge limited emission regime, the ion energy gained inside the sheath in general increases with T_e so the total ion energy increases even further in this configuration because the line of force passing through point #2, and running along the wall, is associated with a high T_e. The same arguments apply to the configuration in the right of Fig. 16. Note that the left configuration in this figure resembles magnetic field topology in conventional Stationary Plasma Thrusters (SPT) whereas the one to the right is more representative of the more modern thrusters like the 6-kW laboratory thruster. Then, based on

these arguments, the configuration at the right in Fig. 15 establishes a more effective magnetic shielding. We note that in this configuration the contribution of $T_e \ln(n_e)$ to the reduction of the plasma potential along the line of force that grazes the wall is small because T_e is low and the plasma potential at the centerline is high. Thus, the expected drop of the plasma potential due to the drop of the plasma density along the diverging wall is not significant. However, it is significant in the configurations of Fig. 16.

In summary, the numerical simulations have shown that the particular topology and magnitude of the magnetic field near the diverging walls of the BPT-40000 in its steady-state configuration had the following consequences:

1) reduction of the accelerating electric field parallel to the wall, prohibiting ions from acquiring significant impact kinetic energy before entering the sheath,

2) reduction of the potential fall in the sheath along the wall, further diminishing the total impact energy that ions could gain before striking the material and,

3) reduction of the ion number density decreasing the flux of ions to the wall.

In support of these conclusions the reader is also referred to the contoured plots of Fig. 13. The computed reductions for all ion species have been presented in Tables 2 and 3. Here, for illustration, we also plot some of the tabulated results in Fig. 17. The results show that the largest effects on the erosion were due to the lower total energy and flux of ions striking the wall. Regarding the effects of the incidence angle, we found them not to affect the erosion rate comparisons as significantly. The bar plots for the incidence angle and erosion rates at the outer wall are provided in Fig. 17 bottom-middle and bottom-right, respectively.

---TABLE---

Table 2. Erosion rates and relevant parameters at the <u>outer</u> wall in the 1200-h and steady-state (SS) channel geometries of the BPT-4000.

--TABLE---

Table 3. Erosion rates and relevant parameters at the <u>inner</u> wall in the 1200-h and steady-state (SS) channel geometries of the BPT-4000.

Regarding the effects of uncertainties in the plasma solution (as discussed in Section III-B) on the erosion rates, we note that the overall trend of the plasma potential inside the acceleration channel cannot be significantly different from the computed profile; Hall thrusters like the BPT-4000 operate with the highest potential regions near the anode and the lowest potential regions in the exhaust. Because in the steady-state configuration of the BPT-4000 the magnetic field streamline that grazes the corner formed by the cylindrical and diverging sections of the wall extends deep into the channel, it will be a line that is conclusively associated with high potentials. It is therefore marginally subject to the uncertainties of the plasma model. Since the fundamental principle that leads to the equipotentialization of the lines leads also to their isothermalization the arguments made about the plasma potential profile near the diverging section apply also to the electron temperature. That is, the grazing line of force is also a low-temperature line. Finally, regarding the plasma density, it should be noted that the number of charged particles is likely much higher in the high-divergence regions of the channel and in the large-angle plume of the thruster than the values presently predicted by Hall2De. This is also suggested by the comparisons between theory and experiment in Section III-A. As also discussed however in Section III-B, the uncertainty of Hall2De's plasma predictions is highest at the downstream point of the diverging walls and decreases as the upstream point is approached. A comparison of the erosion rates at location "D" (see Tables 2 and 3 and Fig. 17) suggests a

difference that exceeds 5 orders of magnitude. Thus, even if the true plasma density was higher by two orders of magnitude in the steady-state geometry than the value predicted by Hall2De, and if the density in the 1200-h geometry remained unchanged, there would still be at least a three-order-of-magnitude reduction in the erosion rates at these locations of the walls.

---FIGURE--

Fig. 17. Bar plots of the erosion rates and relevant parameters at three locations on the outer wall of the BPT-4000 acceleration channel. The values shown here are for singly-charged ions only. Results for all ion charge states are shown in Tables 2 and 3 for the outer and inner walls, respectively.

V. Conclusion

This paper provided possible explanations of the physics that led to the significantly-reduced erosion of the channel in a Hall plasma accelerator upon completion of a >10,000-h QLT. The explanations have been based on 2-D axisymmetric simulations that were performed using the MFAM plasma solver Hall2De.

Several plasma and performance measurements were obtained in this thruster. Comparisons with the simulation results have shown that the agreement is within the experimental uncertainty for the majority of the comparisons we performed. In cases where the simulation results were outside the experimental uncertainty we have identified the likely sources of discrepancy and assessed the impact of these discrepancies on our erosion predictions.

We have found that the erosion rate reductions between the two simulated channel configurations - the 1200-h and the steady-state geometries - were different by many orders of magnitude at certain locations along the walls. Based on the range of comparisons performed with the plasma measurements, foreseeable improvements to our plasma models are not expected

to yield differences between the two channel geometries that exceed one order of magnitude. Thus, we conclude that the shielding of the channel surfaces was indeed enabled by the specific topology of the magnetic field as suggested by our plasma simulations.

The implications of magnetic shielding physics in Hall thrusters are potentially breakthrough. As our numerical simulations suggest, by properly shaping the magnetic field near the acceleration channel walls their erosion can be reduced by several orders of magnitude. Such reductions retire the major risk associated with the use of this electric propulsion technology onboard science missions.

FIGURES

cathode-to-plate
plume boundary

cathode boundary

horizontal far-plume
boundary

dielectric-wall
boundary

vertical far-plume
boundary

anode
boundary

extent of the HPHall
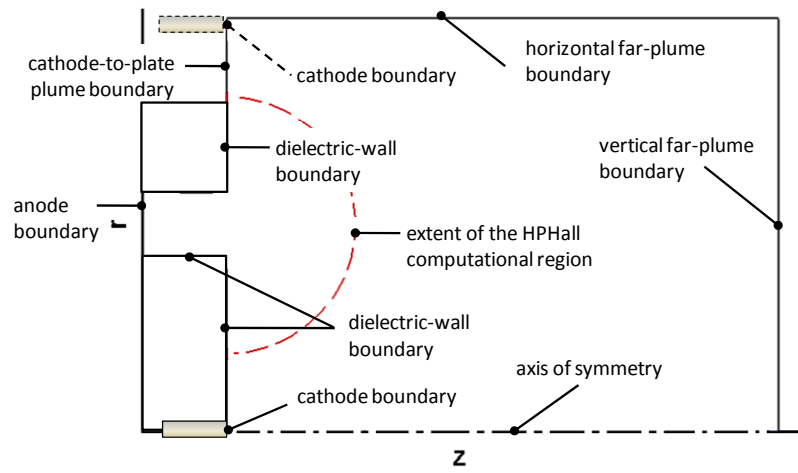computational region

dielectric-wall
boundary

axis of symmetry

cathode boundary
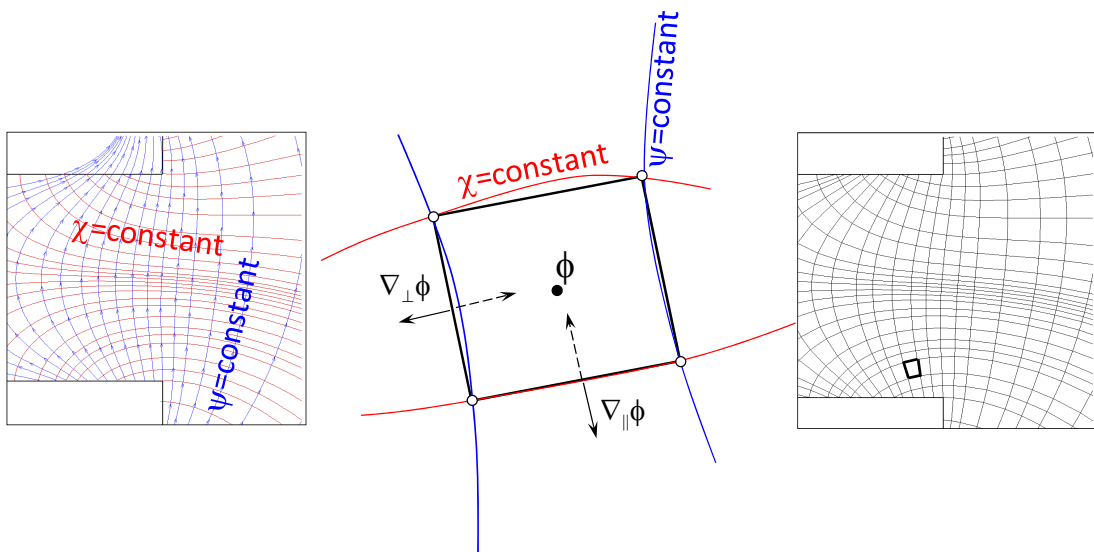
Fig. 1.

Fig. 2. (Color online)

Fig. 3. (Color online)

Cathode

Steady-state channel geometry
1200-h channel geometry
BOL channel geometry

Acceleration channel

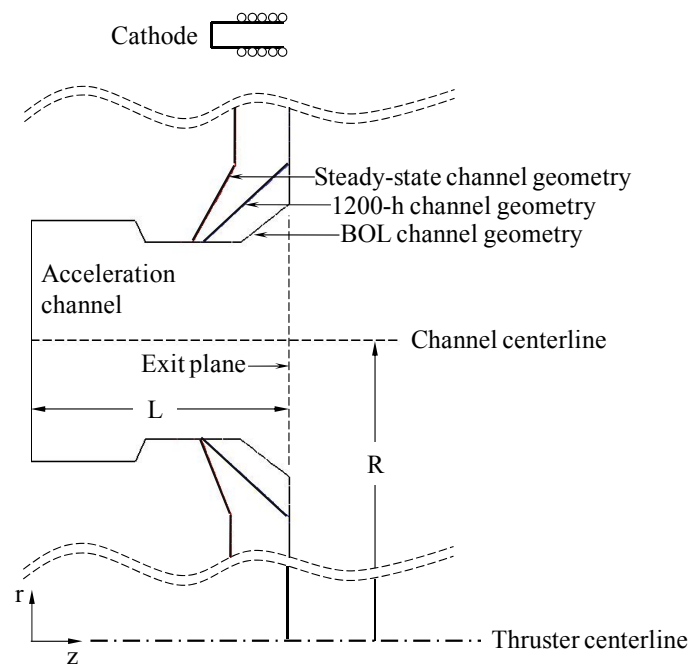Channel centerline

Exit plane

L
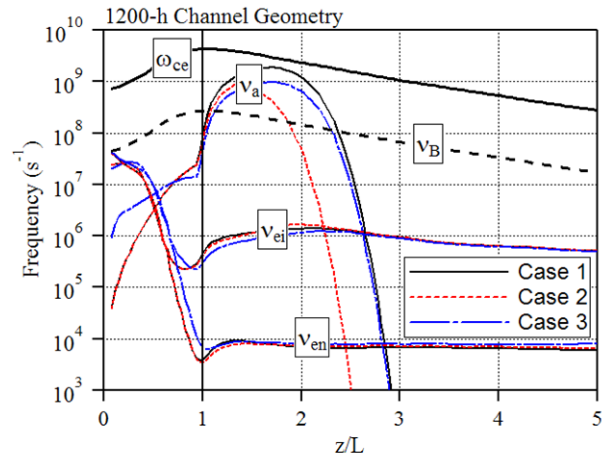
R

r

z
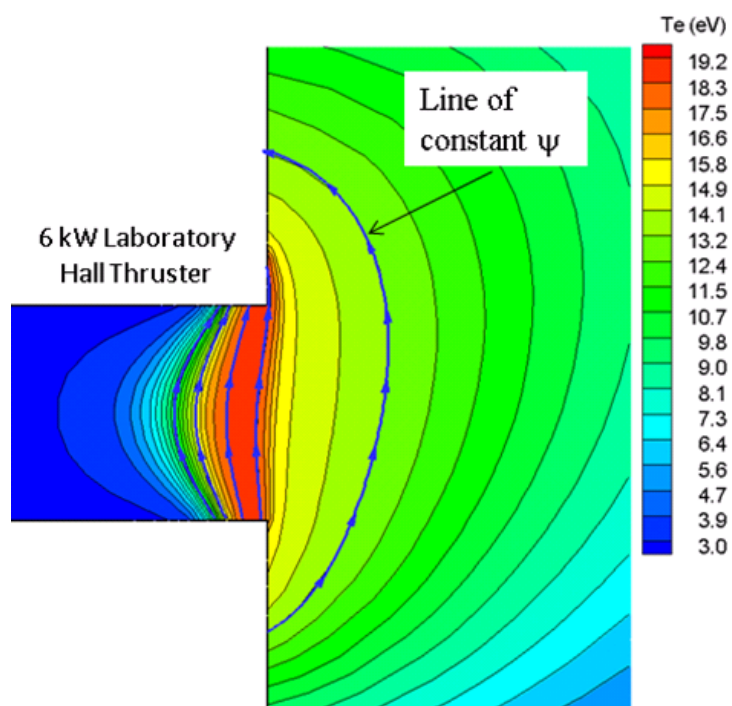
Thruster centerline
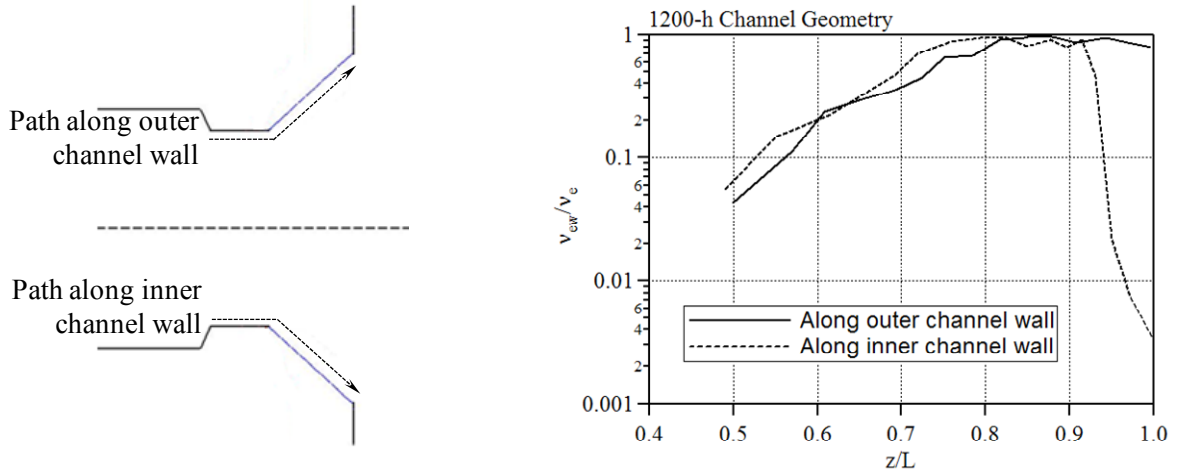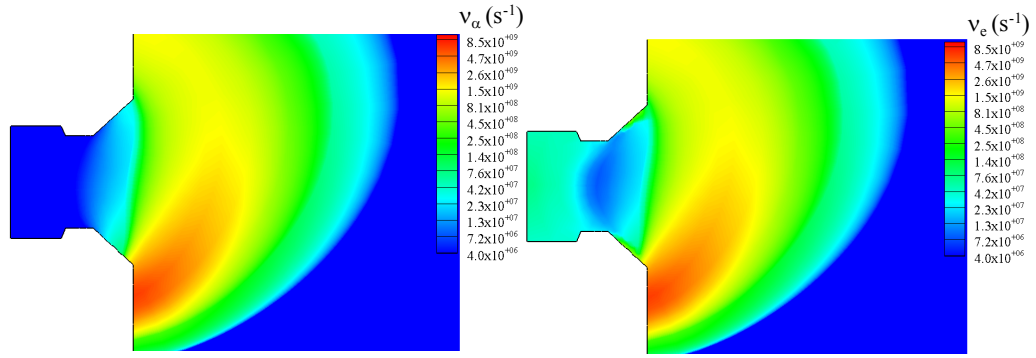
Fig. 4.

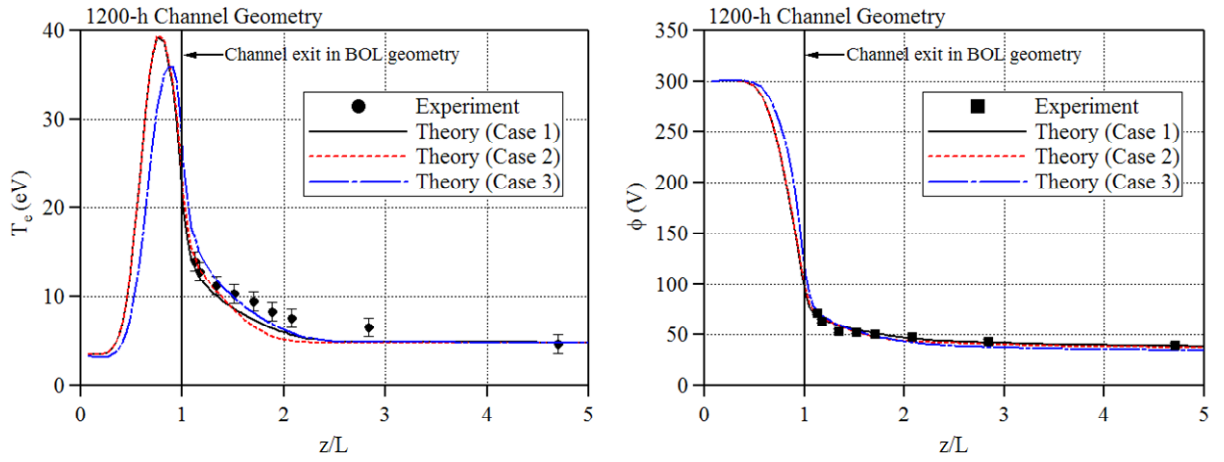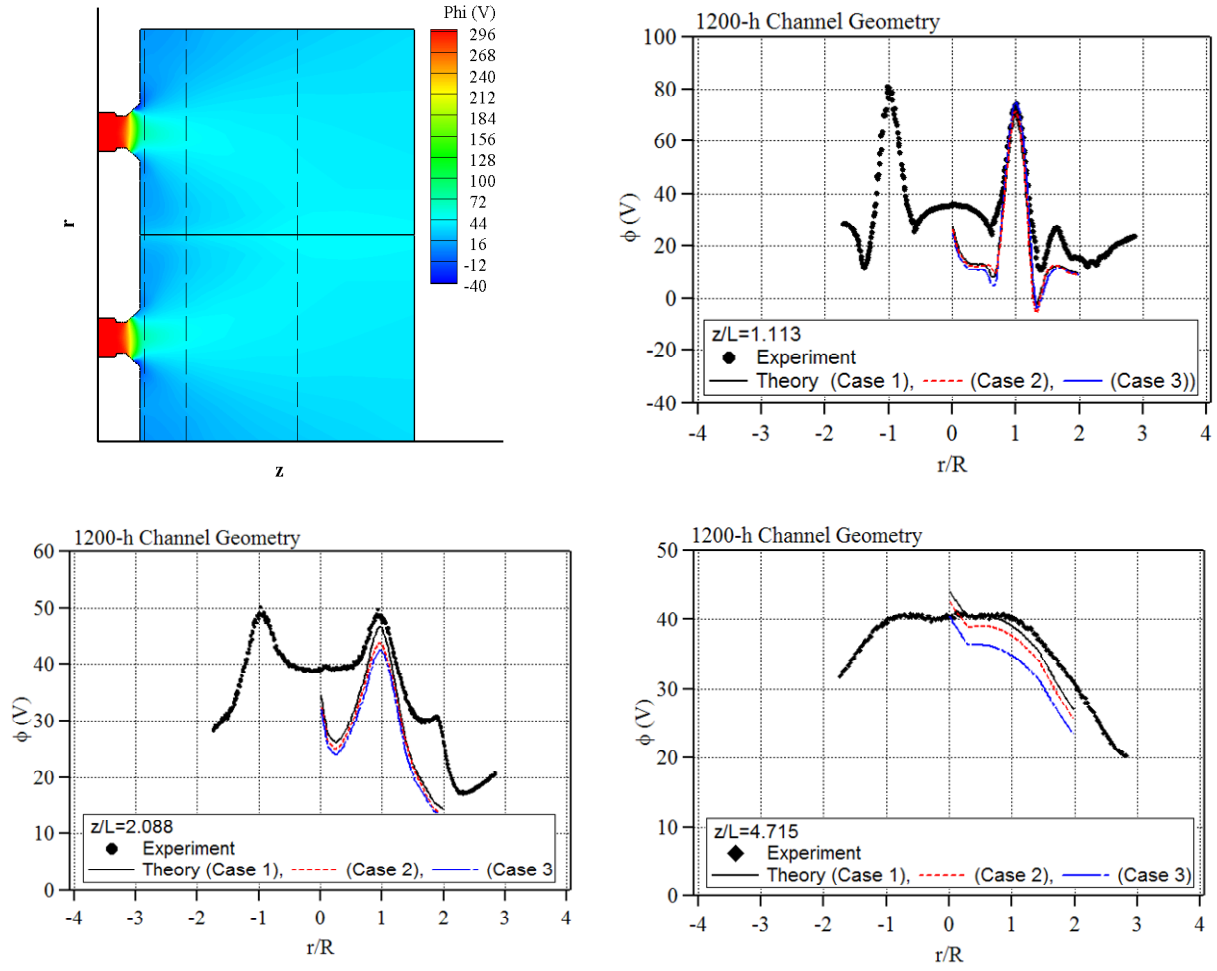Fig. 5. (Color online)

Fig. 6.
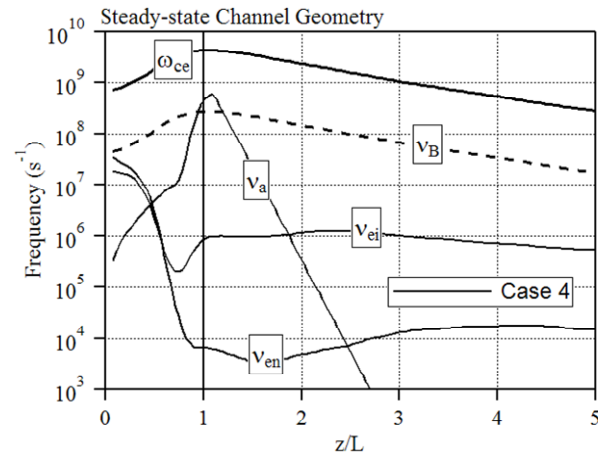
Fig. 7. (Color online)

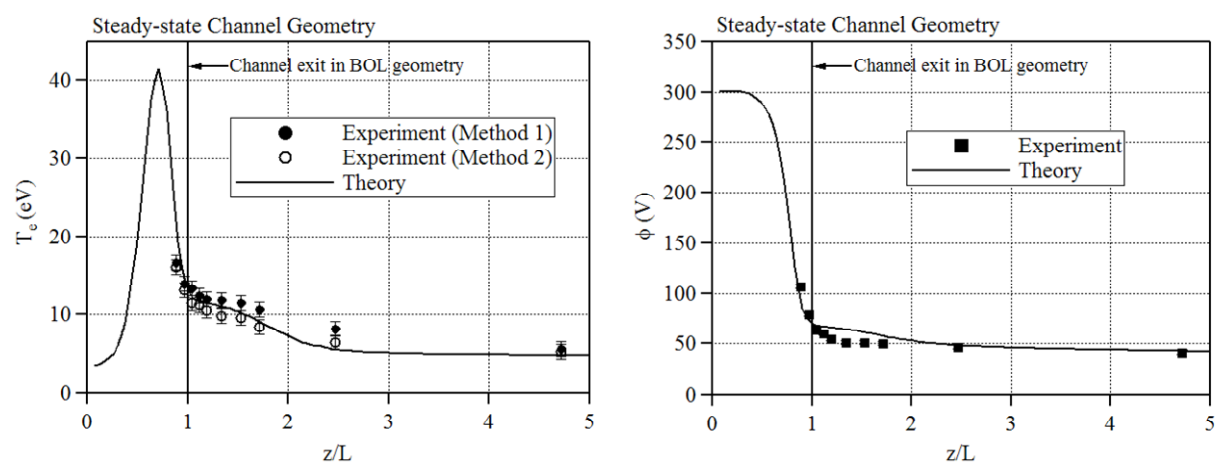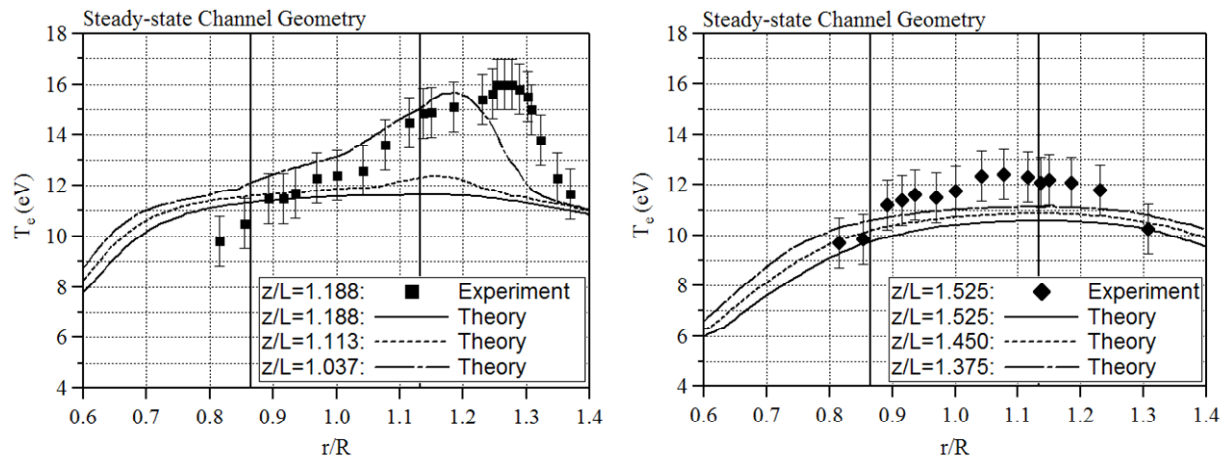
Fig. 8. (Color online)

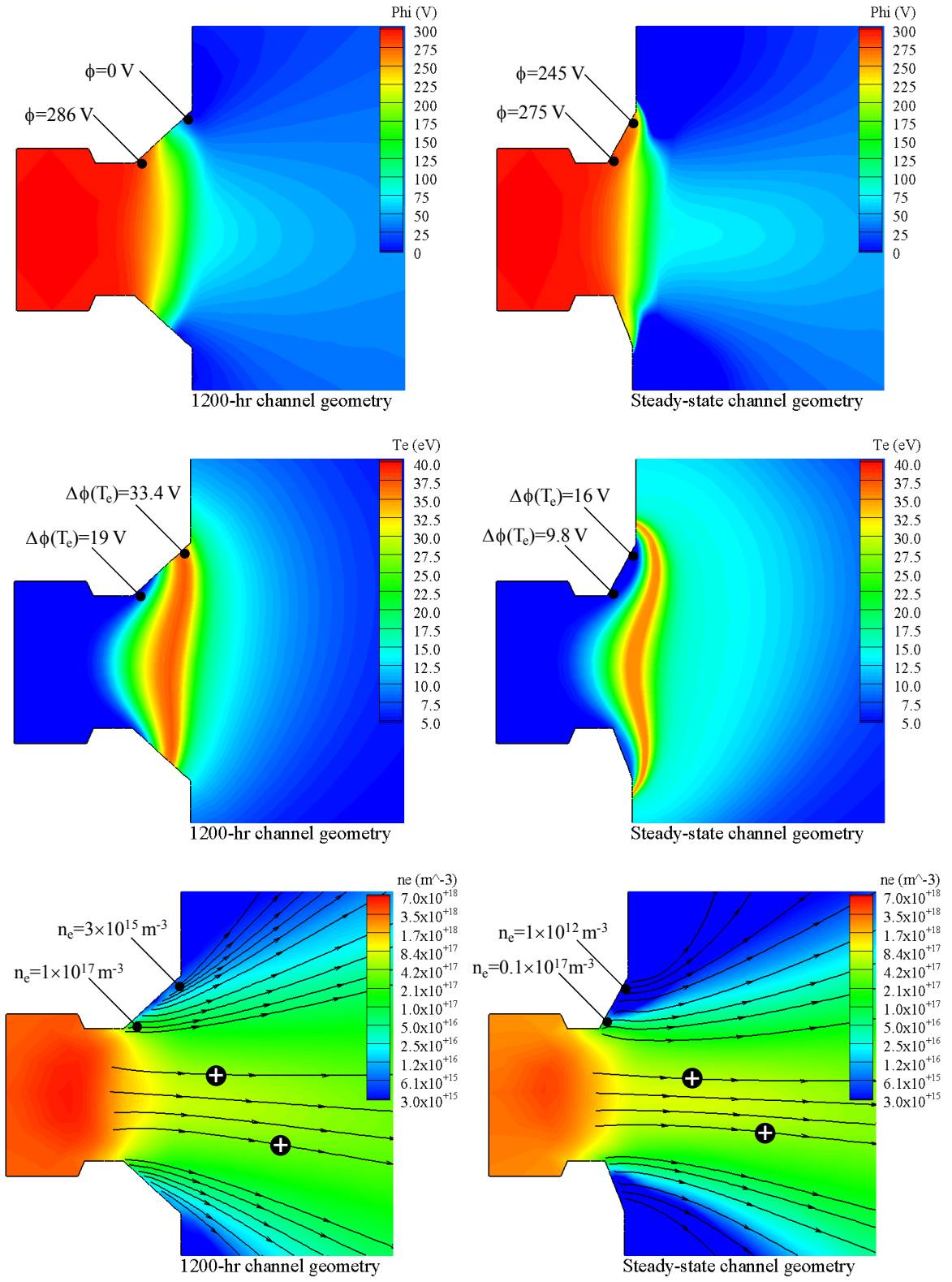Fig. 9. (Color online)

Fig. 10.

Fig. 11.

Fig. 12.

Fig. 13. (Color online)
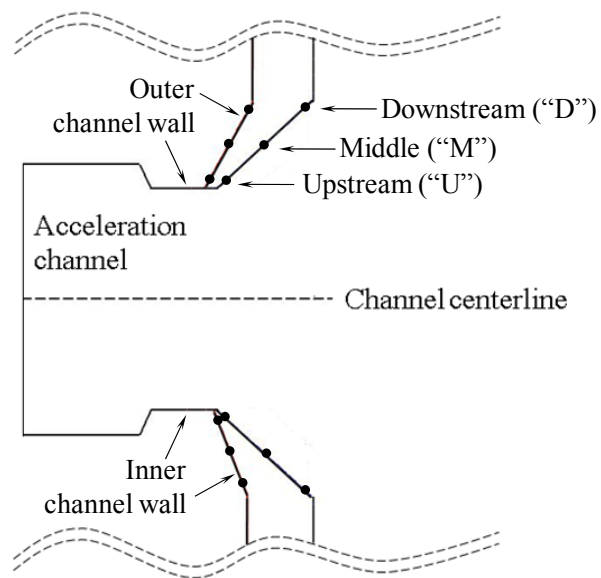
Fig. 14.
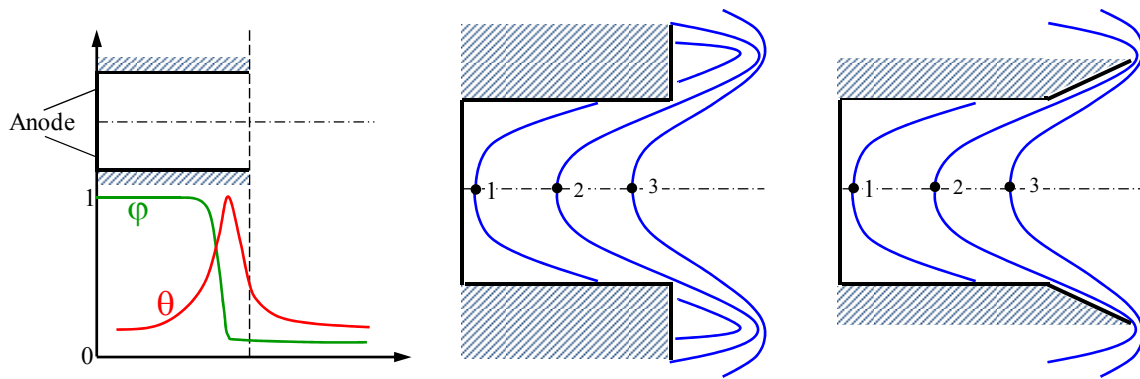
Fig. 15
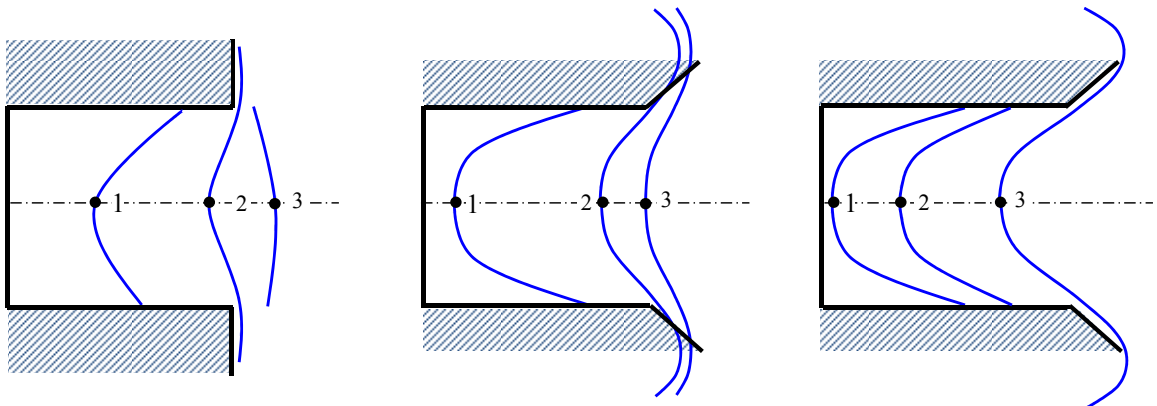
Fig. 16 (Color online)
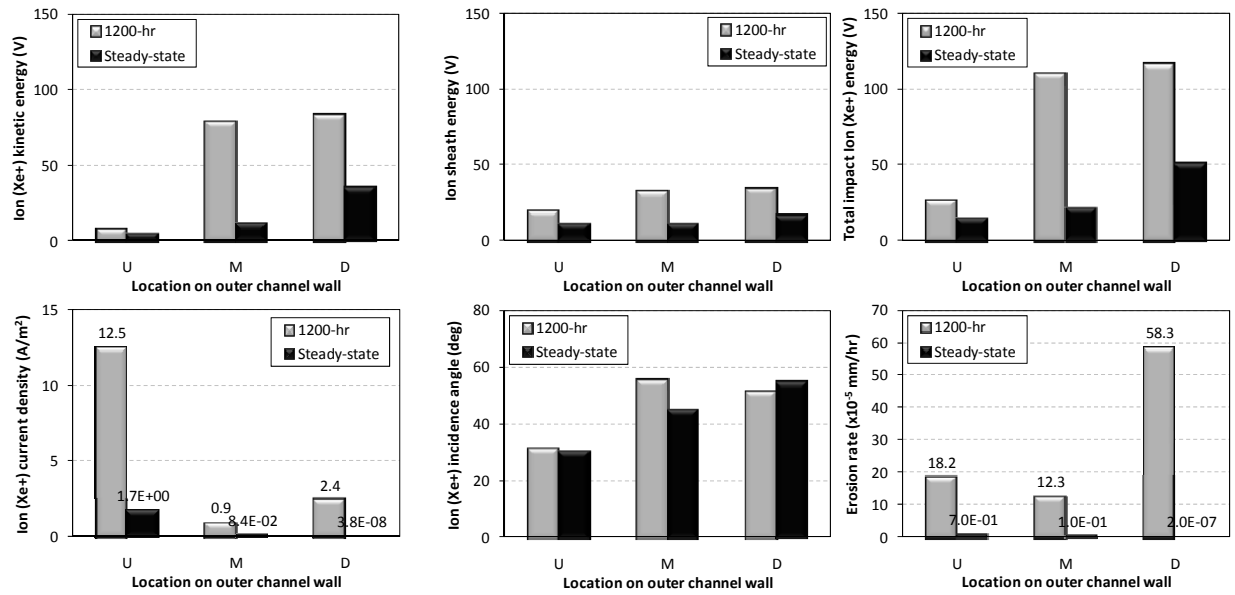
Fig. 17.

TABLES

Table 1.

Channel geometry	1200-h				Steady-state	
Experiment vs. Theory	Experiment	Theory (Case 1)	Theory (Case 2)	Theory (Case 3)	Experiment	Theory (Case 4)
Anode flow rate (mg/s)	14.4	14.4	14.4	14.4	14.5	14.4
Discharge voltage (V)	300	300	300	300	300	300
Discharge current (A)	15	15	15	15	15	15
Thrust (mN)	278.6	274.7	275.0	272.1	280.4	270.9
Beam current, I_b (A)	12.1	12.86	12.87	12.60	12.2-12.3	13.0
Xe^+ current fraction, I_i^+/I_b	0.691	0.644	0.643	0.663	0.696	0.622
Xe^{2+} current fraction, I_i^{2+}/I_b	0.241	0.315	0.316	0.302	0.204	0.332
Xe^{3+} current fraction, I_i^{3+}/I_b	0.054	0.041	0.041	0.034	0.080	0.046
Xe^{4+} current fraction, I_i^{4+}/I_b	0.015	NA	NA	NA	0.021	NA
Mass utilization, η_m	0.952	0.998	0.998	0.990	0.95-0.958	0.987
Current utilization, η_b	0.807	0.857	0.858	0.840	0.813-0.82	0.867

NA=not accounted for in the simulation.

Table 2.

Location along wall	Upstream (U)		Middle (M)		Downstream (D)	
Channel geometry	1200-h (Case 3)	SS (Case 4)	1200-h (Case 3)	SS (Case 4)	1200-h (Case 3)	SS (Case 4)
T_e (eV)	4.5	2.2	18.7	2.2	32.8	3.7
n_i^+ (m^{-3})	1.3×10^{17}	1.1×10^{16}	2.3×10^{15}	6×10^{14}	3.4×10^{15}	2.1×10^{8}
n_i^{2+} (m^{-3})	1.9×10^{15}	7×10^{13}	3×10^{14}	4.7×10^{12}	1.4×10^{15}	1.6×10^{6}
n_i^{3+} (m^{-3})	1.5×10^{12}	3.3×10^{11}	1.4×10^{13}	2.9×10^{10}	2×10^{14}	8.2×10^{-6}
ϕ (V)	285.7	275.1	165.9	269.1	7.0×10^{-2}	245
$j_{i\perp}^+$ (A/m^2)	12.5	1.7	0.9	8.4×10^{-2}	2.4	3.8×10^{-8}
$j_{i\perp}^{2+}$ (A/m^2)	0.5	3×10^{-2}	0.3	2×10^{-3}	2.8	7.5×10^{-10}
$j_{i\perp}^{3+}$ (A/m^2)	6×10^{-4}	2.5×10^{-4}	2.6×10^{-2}	2.2×10^{-5}	0.8	6.7×10^{-21}
$(K/q)_i^+$ (V)	7.2	4.2	78.6	10.8	83.4	34.8
$(K/q)_i^{2+}$ (V)	7.6	6	63.4	13.7	69.7	43.8
$(K/q)_i^{3+}$ (V)	15.1	9.2	52.2	14.8	61.3	51.8
$\Delta\phi$ (V)	19	9.8	31.8	9.8	33.4	16
θ^+ (deg)	31	29.9	55.4	44.6	51.1	54.8
θ^{2+} (deg)	31.6	35.7	52.3	48.3	48.4	58
θ^{3+} (deg)	41.5	42.4	49.4	49.4	46.3	60.3
Y^+ ($\times10^{-2}$ mm^3/C)	0.4	0.1	3.0	0.4	3.0	1.5
Y^{2+} ($\times10^{-2}$ mm^3/C)	0.4	0.2	2.6	0.5	2.6	1.8
Y^{3+} ($\times10^{-2}$ mm^3/C)	0.7	0.3	2.2	0.5	2.3	2.1
ε^+ (mm/h)	1.7×10^{-4}	7×10^{-6}	9.5×10^{-5}	1×10^{-6}	2.6×10^{-4}	2×10^{-12}
ε^{2+} (mm/h)	8×10^{-6}	1.9×10^{-7}	2.6×10^{-5}	3.4×10^{-8}	2.6×10^{-4}	4.8×10^{-14}
ε^{3+} (mm/h)	1.5×10^{-8}	2.7×10^{-9}	2×10^{-6}	4.2×10^{-10}	7.0×10^{-5}	5×10^{-25}
Total ε (mm/h)	**1.8×10^{-4}**	**7×10^{-6}***	**1.2×10^{-4}**	**1×10^{-6}**	**5.8×10^{-4}**	**2×10^{-12}**

Table 3.

Location along wall	Upstream (U)		Middle (M)		Downstream (D)	
Channel geometry	1200-h (Case 3)	SS (Case 4)	1200-h (Case 3)	SS (Case 4)	1200-h (Case 3)	SS (Case 4)
T_e (eV)	6.5	12.1	34.3	9.8	14.6	12.8
n_i^+ (m^{-3})	1.2×10^{17}	4.5×10^{16}	1.6×10^{16}	2×10^{14}	5.6×10^{15}	3.3×10^{10}
n_i^{2+} (m^{-3})	5.1×10^{15}	6.4×10^{15}	3.1×10^{15}	3.1×10^{13}	2.1×10^{15}	8.5×10^{9}
n_i^{3+} (m^{-3})	1.1×10^{13}	2×10^{14}	3×10^{14}	8.7×10^{11}	3×10^{14}	5.2×10^{8}
ϕ (V)	275.9	253.9	116.1	201.8	9.6	136.6
$j_{i\perp}^+$ (A/m^2)	14.1	2	7.5	5.0×10^{-2}	3.0	1.5×10^{-5}
$j_{i\perp}^{2+}$ (A/m^2)	1.9	1.5	4.2	2.4×10^{-2}	3.1	1.1×10^{-5}
$j_{i\perp}^{3+}$ (A/m^2)	7.1×10^{-3}	6.2×10^{-2}	0.8	1.2×10^{-3}	1.0	1.2×10^{-6}
$(K/q)_i^+$ (V)	13.7	15.5	100.9	12.8	74.2	54.5
$(K/q)_i^{2+}$ (V)	11.8	13.5	82.2	18.3	64.4	63.9
$(K/q)_i^{3+}$ (V)	16.6	15.1	65.8	34.9	57.0	73.4
$\Delta\phi$ (V)	26.5	43.1	35.0	37.4	46.5	44.4
θ^+ (deg)	35.2	30.9	56.6	27.6	48.0	44.8
θ^{2+} (deg)	33.0	29	53.7	32.7	45.9	47.3
θ^{3+} (deg)	37.8	30.5	50.3	42.4	43.9	49.4
Y^+ ($\times 10^{-2}$ mm^3/C)	0.7	1	3.7	0.8	2.9	2.3
Y^{2+} ($\times 10^{-2}$ mm^3/C)	0.7	0.9	3.1	1	2.6	2.6
Y^{3+} ($\times 10^{-2}$ mm^3/C)	0.9	1	2.6	1.7	2.4	2.9
ε^+ (mm/h)	3.8×10^{-4}	7.6×10^{-5}	9.9×10^{-4}	1×10^{-6}	3.1×10^{-4}	1.2×10^{-9}
ε^{2+} (mm/h)	4.6×10^{-5}	5.2×10^{-5}	4.8×10^{-4}	8.9×10^{-7}	2.9×10^{-4}	1×10^{-9}
ε^{3+} (mm/h)	2.2×10^{-7}	2×10^{-6}	7.6×10^{-5}	7.4×10^{-8}	8.2×10^{-5}	1.3×10^{-10}
Total ε (mm/h)	**4.3×10^{-4}**	**1.3×10^{-4} ***	**1.5×10^{-3}**	**1×10^{-6}**	**6.9×10^{-4}**	**2.2×10^{-9}**

* This erosion rate is an overestimate of the real value in the BPT-4000 QLT because the numerical simulation geometry employs a sharp corner at this location whereas in the real geometry this corner was smoothed out by the erosion. The significance of this difference is that in the simulation the corner "interrupts" magnetic field streamlines leading to potential differences around the corner that allow ions to acquire kinetic energy. By contrast, the curvature of the eroded corner in the test follows closely the curvature of the streamline around that corner; the equipotentialization of the streamline reduces the acceleration of the ions around the corner and, in turn, the kinetic energy with which they impact the surface of the thruster.

References

[1] D. Y. Oh, *J. Spacecraft Rockets*, 44, 2, 399-411 (2007).

[2] R. R. Hofer, T. M Randolph, D. Y. Oh, J. S. Snyder, K. H. de Grys, AIAA Paper No. 06-4469 (American Institute of Aeronautics and Astronautics, Washington, D.C., 2006).

[3] D. T. Jacobson, D. H. Manzella, U.S. Patent Application for "Elimination of Lifetime Limiting Mechanism of Hall Thrusters," Application No. 11/044,471, filed 28 Jan. 2005, Patent No. 7500350, issued 10 March 2009.

[4] H. Kamhawi, D. H. Manzella, L. Pinero, T. Haag, A. Mathers, and H. Liles, AIAA Paper No. 09-5282 (American Institute of Aeronautics and Astronautics, Washington, D.C., 2009).

[5] H. Kamhawi, D. H. Manzella, and P. Peterson, JANNAF, Proceedings of the 6th MSS, 4th LPS, 3rd SPS Joint JANNAF Meeting, Orlando, FL (Chemical Propulsion Information Analysis Center, Columbia, MD, 2008) Paper No. SPS-III-11.

[6] K. H. De Grys, A. Mathers, B. Welander, and V. Khayms, AIAA Paper No. 10-6698 (American Institute of Aeronautics and Astronautics, Washington, D.C., 2010).

[7] D. Q. King, K. H. de Grys, R. S. Aadland, D. L. Tilley, and A. W. Voigt, "Magnetic Flux Shaping in Ion Accelerators with Closed Electron Drift," US Patent 6,208,080, 27 March 2001.

[8] K. H. De Grys, B. Welander, J. Dimicco, S. Wenzel, B. Kay, V. Kayms, and J. Paisley, AIAA Paper No. 05-3682, (American Institute of Aeronautics and Astronautics, Washington, D.C., 2005).

[9] J. M. Fife, "Hybrid-PIC modeling and electrostatic probe survey of Hall thrusters," Ph.D. thesis, Massachusetts Institute of Technology, 1998.

[10] F. I. Parra, E. Ahedo, J. M. Fife, and M. Martinez-Sanchez, *J. Appl. Phys.*, 100, 023304 (2006).

[11] M. Gamero-Castaño, and I. Katz, Proceedings of the 29th International Electric Propulsion Conference, Princeton, NJ (Electric Rocket Propulsion Society, Fairview Park, OH, 2005), IEPC Paper No. 05-303.

[12] R. R. Hofer, I. G. Mikellides, I. Katz, and D. M. Goebel, Proceedings of the 30th International Electric Propulsion Conference, Florence, Italy (Electric Rocket Propulsion Society, Fairview Park, OH, 2007), IEPC Paper No. 07-267.

[13] R. R. Hofer, I. Katz, I. G. Mikellides, D. M. Goebel, K. K. Jameson, R. M. Sullivan, and L. K. Johnson, AIAA Paper No. 08-4924 (American Institute of Aeronautics and Astronautics, Washington, D.C., 2008).

[14] I. G. Mikellides, I. Katz, R. R. Hofer, and D. M. Goebel, Proceedings of the 31st International Electric Propulsion Conference, Ann Arbor, MI (Electric Rocket Propulsion Society, Fairview Park, OH, 2009), IEPC Paper No. 09-114.

[15] I. G. Mikellides, I. Katz, D. M. Goebel, K. K. Jameson, and J. E. Polk, *J. Propul. Power*, 24, 866 (2008).

[16] I. G. Mikellides, and I. Katz, *J. Propul. Power*, 24, 855 (2008).

[17] R. R. Hofer, D. M. Goebel, J. S. Snyder, and I. Sandler, Proceedings of the 31st International Electric Propulsion Conference, Ann Arbor, MI (Electric Rocket Propulsion Society, Fairview Park, OH, 2009), IEPC Paper 09-85.

[18] A. I. Morozov, and V. V. Savelyev, *Reviews of Plasma Physics*, 21, 203 (2000).

[19] R. Marchand, and M. Dumberry, *Computer Physics Communications*, 96, 232 (1996).

[20] Z. Lin, T. S. Hahm, W. W. Lee, W. M. Tang, and R. B. White, *Science*, 281, 1835 (1998).

[21] A. M. Dimits, *Physical Review E*, 48, 4070 (1993).

[22] M. J. LeBrun, T. Tajima, M. G. Gray, G. Furnish, and W. Horton, *Physics of Fluids B*, 5, 752 (1993).

[23] R. Marchand, J. Y. Lu, K. Kabin, and R. Rankin, *Advanced Methods for Space Simulations*, eds Usui, H. and Omura, Y., Terrapub, Tokyo, pp. 111–143 (2007).

[24] W. Huang, B. Drenkow, and A. D. Gallimore, AIAA Paper No. 09-5355 (American Institute of Aeronautics and Astronautics, Washington, D.C., 2009).

[25] A. Müller, "Experimental Cross Sections for Electron-Impact Ionization and Electron-Ion Recombination," Research Coordination Meeting, IAEA CRP, Vienna, March 04-06, 2009http://www-dis.iaea.org/CRP/Heavy_elements/Presentations3/Mueller.pdf

[26] K. Riemann, J. Phys. D: Appl. Phys. 24, 493 (1991).

[27] K. Riemann, IEEE Trans. Plasma Sci. 23, 709 (1995).

[28] E. Ahedo and R. Santos, Phys. Plasmas 17, 073507 (2010).

[29] A. Ducrocq, J. C. Adam, A. Héron, and G. Laval, Phys. Plasmas 13, 102111 (2006)

[30] A. Lazurenko, T. Dudok de Wit, C. Cavoit, V. Krasnoselskikh, A. Bouchoule, and M. Dudeck, Phys. Plasmas 14, 033504 (2007).

[31] C. Boniface, L. Garrigues, G. J. M. Hagelaar, J. P. Boeuf, D. Gawron, and S. Mazouffre, Appl. Phys. Lett. **89**, 161503 (2006)

[32] D. Bohm, E. Burhop, and H. Massey, *Characteristics of Electrical Discharges in Magnetic Fields* (McGraw-Hill, New York, 1949), p. 77.

[33] S. I. Braginskii, *Reviews of Plasma Physics*, (Consultants Bureau, New York, 1965), Vol. 1, p. 205.

[34] I. G. Mikellides, I. Katz, R. R. Hofer, D. M. Goebel, K. H. de Grys, and A. Mathers, AIAA Paper No. 10-6942 (American Institute of Aeronautics and Astronautics, Washington, D.C., 2010).

[35] I. G. Mikellides, and I. Katz, Proceedings of the 30th International Electric Propulsion Conference, Florence, Italy (Electric Rocket Propulsion Society, Fairview Park, OH, 2007), IEPC Paper 07-18.

[36] I. G. Mikellides, I. Katz, D. M. Goebel, and J. E. Polk, *J. Appl. Phys.*, 98, 113303 (2005).

[37] G. D. Hobbs, and J. A. Wesson, *Plasma Phys.*, 9, 85 (1967).

[38] B. M. Reid, A. D. Gallimore, R. R. Hofer, Y. Li, J. M. Haas, Proceedings of the 54th JANNAF Propulsion Meeting, Denver, CO, (Chemical Propulsion Information Analysis Center, Columbia, MD, 2007).

[39] J. M. Haas, R. R. Hofer, D. L. Brown, B. M. Reid, A. D. Gallimore, Proceedings of the 54th JANNAF Propulsion Meeting, Denver, CO, (Chemical Propulsion Information Analysis Center, Columbia, MD, 2007).

[40] D. L. Brown, B. M. Reid, A. D. Gallimore, R. R. Hofer, J. M. Haas, and C. W. Larson, Proceedings of the 54th JANNAF Propulsion Meeting, Denver, CO, (Chemical Propulsion Information Analysis Center, Columbia, MD, 2007).

[41] I. Katz, and I. G. Mikellides, J. Comput. Phys. (2010), doi:10.1016/j.jcp.2010.11.013.

[42] G. Hagelaar, J. Bareilles, L. Garrigues, and J. P. Boeuf, *J. Appl. Phys.,* 91, 5592 (2002).

[43] J. Bareilles, G. Hagelaar, L. Garrigues, C. Boniface, and J. Boeufa, *Phys. Plasmas*, 11, 6 (2004).

[44] I. Katz, R. R. Hofer, D. M. Goebel, *IEEE Trans. Plasma Sci.,* 36, 2015 (2008).

[45] M. S. McDonald, and A. D. Gallimore, Proceedings of the 31st International Electric Propulsion Conference, Ann Arbor, MI (Electric Rocket Propulsion Society, Fairview Park, OH, 2009), IEPC Paper No. 09-113.

[46] S. Barral, K. Makowski, Z. Peradzynski, N. Gascon, and M. Dudeck, *Phys. Plasmas*, 10, 4137 (2003).

[47] Y. Raitses, D. Staack, M. Keidar, and N. J. Fisch, *Phys. Plasmas*, 12, 057104 (2005).

[48] E. Ahedo, and F. I. Parra, *Phys. Plasmas* 12, 073503 (2006).

[49] F. Taccogna, S. Longo, M. and Capitelli, *Phys. Plasmas*, 12, 093506 (2005).

[50] E. Ahedo, *Phys. Plasmas*, 9, 4340 (2002).

[51] R. R. Hofer, I. G. Mikellides, I. Katz, and D. M. Goebel, AIAA Paper No. 07-5267 (American Institute of Aeronautics and Astronautics, Washington, D.C., 2007).

[52] Y. Yamamura, and H. Tawara, Atomic Data and Nuclear Data Tables 62, 149 (1996).

[53] E. Pencil, T. Randolph, and D. H. Manzella, AIAA Paper No. 96-2709 (American Institute of Aeronautics and Astronautics, Washington, D.C., 1996).

[54] G. Kornfeld, N. Koch, H. Harmann, Proceedings of the 30th International Electric Propulsion Conference, Florence, Italy (Electric Rocket Propulsion Society, Fairview Park, OH, 2007), IEPC Paper No. 07-108.

[55] D. G. Courtney, P. Lozanoy, and M. Martinez-Sanchez, AIAA Paper No. 08-463 (American Institute of Aeronautics and Astronautics, Washington, D.C., 2008).